GEOPHYSICS, VOL. 77, NO. 4 (JULY-AUGUST 2012); P. 1–9, 8 FIGS., 1 TABLE.
10.1190/GEO2011-0375.1

# Progressing from 1D to 2D and 3D near-surface airborne electromagnetic mapping with a multisensor, airborne sea-ice explorer

Andreas A. Pfaffhuber[1], Stefan Hendricks[2], and Yme A. Kvistedal[1]

## ABSTRACT

The polar ocean's sea ice cover is an unconventional and challenging geophysical target. Helicopter-electromagnetic (HEM) sea-ice thickness mapping is currently limited to 1D interpretation due to traditional procedures and systems. These systems are mainly sensitive to layered structures, ideally set for the widespread flat (level) ice type. Because deformed sea ice (e.g., pressure ridges) is 3D and usually also heterogeneous, ice thickness errors up to 50% can be observed for pressure ridges using 1D approximations for the interpretation of HEM data. We researched a new generation multisensor, airborne sea ice explorer (MAiSIE) to overcome these limitations. Three-dimensional finite-element modeling enabled us to determine that more than one frequency is needed, ideally in the range 1–8 kHz, to improve thickness estimates of grounded sea-ice pressure ridges that are typical of 3D sea ice structures. With the MAiSIE system, we found a new electromagnetic concept based on one multifrequency transmitter loop and a 3C receiver coil triplet with active digital bucking. The relatively small weight of the EM components freed enough payload to include additional scientific sensors, including a cross-track lidar scanner and high-accuracy inertial-navigation system combined with dual-antenna differential GPS. Integrating the 3D ice-surface topography obtained from the lidar with the EM data at frequencies from 500 Hz to 8 kHz in $x$-, $y$-, and $z$-directions, significantly increased the accuracy of sea-ice pressure-ridge geometry derived from HEM data. Initial test flight results over open water showed the proof-of-concept with acceptable sensor drift and receiver sensitivity. Noise levels were relatively high (20–250 parts-per-million) due to unwanted interference, leaving room for optimization. The 20 ppm noise level at 4.1 kHz is sufficient to map level ice thickness with 10 cm precision for sensor altitudes below 13 m.

## INTRODUCTION

Detailed observation and accurate mapping of the cryosphere, especially during periods of noticeable climate change, is possibly one of the biggest scientific challenges currently facing researchers (ACIA 2004). One key data set for climate studies is sea-ice volume and its interannual variation (e.g., Singarayer et al., 2006). Airborne electromagnetic (AEM) surveys have been playing an increasingly large role in this field, because they are the only geophysical method currently capable of directly measuring ice thickness (e.g., Lindsay, 2010). With the work presented here, we strive to improve the versatility and accuracy of AEM methods for determining sea-ice thickness in a 3D environment.

Extensive use of surface-based electromagnetic (EM) for ice-thickness profiling (Kovacs and Morey, 1991) was triggered by initial work in the 1970s (Sinha, 1976) and later provided the proof-of-concept for AEM developments. Regional mapping of the sea-ice thickness distribution using HEM began in the late 1980s in North America with traditional exploration systems (Kovacs et al., 1987), later leading to sea-ice dedicated devices (Kovacs and Holladay 1990). This technology was further developed in Canada (Holladay et al., 1990; Prinsenberg et al., 2002) prior to research in Europe since the early 1990s. The first European airborne EM sea-ice field program was conducted in the Baltic Sea using the Geological Survey of Finland's fixed-wing EM system (Multala et al., 1996). In the late 1990s, the German Alfred Wegener Institute for Polar and Marine Research (AWI) developed a sea ice HEM system, which is a small, fully digital instrument that has been used on an operational basis during ship- and land-based expeditions in the Arctic, Antarctic, and Baltic Seas (Pfaffling et al., 2004; Haas et al., 2006).

Manuscript received by the Editor 30 September 2011; revised manuscript received 28 February 2012.
[1]Norwegian Geotechnical Institute, Oslo, Norway. E-mail: aap@ngi.no; yk@ngi.no.
[2]Alfred Wegener Institute for Polar and Marine Research, Bremerhaven, Germany. E-mail: stefan.hendricks@awi.de.
© 2012 Society of Exploration Geophysicists. All rights reserved.

The state of the art in AEM sea-ice thickness mapping is twofold. (1) Based on the original developments mentioned above, the Canadian Department of Fisheries and Oceans (DFO) is operating helicopter-mounted and helicopter-towed systems through DFO's Bedford Institute of Oceanography and the Canadian Coast Guard on an operational basis. These systems are utilizing multiple frequencies and EM geometries, acquire pitch and roll data and provide sea-ice thickness and conductivity as final inversion results. DFO systems are to our knowledge strictly used for assisting ice charting and monitoring initiatives within the Canadian Arctic. (2) In the field of global climate research, however, a simplified one-to-two-frequency system has become a state-of-practice platform based on the original AWI system, and has recently been adapted by the University of Alberta (Canada), the Norwegian Polar Institute, and the Polar Research Institute of China. In the following, we refer to these simplified systems as current systems.

Detailed studies on the accuracy of AEM ice-thickness data have revealed certain limitations. Fundamental limitations are governed by the technology of current, simple, sea-ice AEM devices. Several authors have addressed the effect of bird motion (attitude) for AEM in general (Fitterman and Yin, 2004; Davis et al., 2006), and also for using AEM to measure sea-ice thickness (Holladay and Prinsenberg, 1997). Most sea ice systems don't measure pitch and roll, thereby making it difficult to correct for attitude errors.

Further, standard 1D data processing tends to underestimate ice thickness for non-1D regions such as pressure ridges. Pressure ridges are porous, blocky structures formed in deformation events when two convergent ice floes break due to lateral stress. These ridges may exceed thicknesses of 25 m, contribute to the thickest sea ice, and present a hazard for commercial operations. They also govern the stability of the land-fast sea-ice zone close to the coast when grounded ridges and their blocky structures result in a large ice-water interface, which might trigger ice melting in summer. We show, with 3D modeling examples, that ridge thickness may be underestimated by up to 50%. Simple sea-ice systems provide horizontal coplanar (HCP) data only. Because the HCP configuration is mostly sensitive to horizontally layered structures, further EM orientations are needed as input data for 2D or 3D interpretation (Reid et al., 2003). Three-dimensional inversion of purely HCP AEM data provided by traditional systems only would lead to minor improvements in determining the thickness of sea-ice ridges. Liu and Becker (1990) based an approximate 2D inversion on vertical coaxial data, and later achieved limited lateral resolution with 2D inversion based on HCP data (Liu et al., 1991).

We present a new generation system, the multisensor airborne sea ice explorer (MAiSIE) that was developed to overcome the limitations associated with traditional, simple sea-ice AEM systems. MAiSIE comprises a multifrequency and multicomponent EM induction system accompanied by high-accuracy attitude sensors and three onboard laser devices (altimeter, IR thermometer, and cross-track lidar scanner). Initial trials data recorded over open water provide us with noise figures that can be directly related to ice-thickness uncertainties, thereby showing that MAiSIE has the potential to initiate a second generation of sea-ice systems, and that it will significantly improve the accuracy of sea-ice thickness estimated from AEM data.

## SEA-ICE GEOPHYSICS

### From EM data to ice thickness

EM data provide a measure on the conductivity and distance of any conductor within range of the emitted EM-field and receiver sensitivity. This conductor ranging capability makes EM ideal for sea-ice thickness retrieval. Saline seawater is a good conductor (2.5–3 S/m) and therefore provides a strong EM response. In contrast, sea ice has a low conductivity, around 0.01 S/m; thus, the measured EM response depends mainly on the height of the system above the seawater. It is consequently possible to directly explore ice thickness with an airborne EM instrument. The basic principle of HEM sea-ice thickness profiling is to estimate the distance to the ice/water interface from the EM data, while a laser altimeter in the towed instrument (bird) determines the system height above the ice or snow surface. The difference of these two distances consequently corresponds to the ice (or ice + snow) thickness. Whenever sea-ice thickness is mentioned in an EM context, it actually refers to the total thickness — meaning ice thickness plus snow thickness. We provided a detailed description and discussion of AEM ice thickness retrieval in Pfaffling and Ried (2009) and Pfaffling et al. (2007).

HEM sea-ice data processing is strictly 1D, leading to a general thickness underestimation of 2D or 3D structures such as pressure ridge by 50% or even more, depending on the assumed ridge shape. Reid et al. (2003) find the maximum HEM derived thickness to be 40%–60% of the true thickness while Hendricks (2009) results range from 50% to 80% of the model, depending on ridge thickness for typical parameters. In a worst-case scenario (large ridge, high ridge porosity, and high instrument altitude) even an 80% mismatch is possible. However, for typical conditions an underestimation of up to 50% can be assumed.

#### *Laser altimetry*

The standard design of current sea-ice HEM systems includes a single-beam laser altimeter for ranging from the sensor to the top ice surface. The altimeter operates at a recording frequency ten times higher than the EM sampling and is filtered to match an average of the EM along-track footprint. This EM footprint is defined as the area where most (90%) of the induction process in the seawater takes place, which is defined by an area with a side length of roughly 40 m (for a system height of 10–15 m). Because a single-beam altimeter does not yield any distance information across-track in regions where the EM reading might still be influenced by the ice topography, an uncertainty is introduced in the ice-thickness estimate. This uncertainty can be reduced by using a lidar scanner which covers the surface topography across the flight track. This method is more demanding in terms of data volume, and requires precise attitude information. The selected instrument (Riegl VQ580) has an opening angle of 60° and can perform up to 150 linear cross-track scans per second. The opening angle will allow a swath width of approximately 17 m at an altitude of 15 m. The minimum altitude of data acquisition is 10 m. To avoid interference between the two sensors, the wavelengths of the single-beam altimeter and scanner are roughly 160 nm apart from each other.

Such lidar scanning systems are currently in use from airplanes for sea-ice topography mapping and the validation of space-borne

sea-ice thickness retrievals. Satellites such as ICESat (Kwok and Cunningham, 2008) and CryoSat-2 (Wingham et al., 2006) measure freeboard (i.e., the height of the sea-ice surface above water level), which can be converted into ice thickness with assumptions of ice density and snow properties. This conversion is very sensitive to uncertainties in the underlying assumptions, and validation data of coincident ice thickness and freeboard data is needed. HEM systems and airborne lidar scanner systems are currently the only sensor combination which is capable of producing this data set at a meaningful scale for satellite products. In spring 2011, AWI operated an EM-bird in tandem with a high-resolution lidar scanner mounted on a fixed-wing aircraft in the western marginal seas of the western Arctic Ocean. The lidar scanner was mounted on the airplane where bore-sight points and attitude data were available. However, mounting a lidar scanner in the housing of the towed bird itself has several advantages. The use of identical GPS receivers for scanner and EM reduces colocation errors, compared to two sensor platforms with independent GPS units. It also allows data acquisition independent of the scientific payload availability of the aircraft. Furthermore, because the bird operates at an altitude of 10–15 m, a centimeter-scale horizontal resolution can be achieved. Though not directly needed for ice-thickness retrieval, this high-resolution topographic information can be used for studies of the interaction of atmosphere and sea ice. One disadvantage when mounting the scanner inside the bird is the fact that the swath of the lidar scanner does not entirely match the footprint of the EM induction process. The use of a lidar scanner will still improve the result compared to single-beam altimeter. There is information from the across-track elevation of the sea ice, where there was none before. Also, though the EM footprint can encompass a large area, the influence of the ice thickness within the footprint doesn't have a uniform weighting, because it is significantly reduced at the edges, as modeling studies from Beamish (2003), Reid et al. (2006b), and Hendricks (2009) have shown.

## 3D EM modeling

The discussed limitations of current sea-ice HEM instruments and processing techniques led to model investigations of the retrieved ice thickness uncertainties for non-1D sea-ice structures. Hendricks (2009) and Rabenstein et al., (2011) developed a 3D forward-
modeling code to simulate HEM data for 2D and 3D sea-ice structures, and to study the EM-fuselage coupling for a fixed-wing EM system operated by AWI. The model is based on the commercial software package Comsol Multiphysics® and solves the 3D EM problem on unstructured grids using a finite-elements method. The reliability of the 1D assumption for helicopter operations was tested on several 2D and 3D sea-ice structures by 1D inversion of the EM response obtained by the 3D forward model (Hendricks, 2009). The results illustrate that the underestimation of the thickness of pressure ridges is significant and variable over a range of 20%–50%. Modeling results are consistent with findings in the field based on drilling profiles (Pfaffling et al., 2007). The modeling shows that traditional approaches are not capable of resolving the maximum thickness of pressure ridges, nor their porosity. Pressure ridge porosity is governed by seawater-filled voids between broken blocks of level ice for young ridges. Pressure ridge keels are thus more conductive than level ice. Over time, some of the ridge keel melts and some of the included water freezes until the ridge consolidates to a more homogeneous ice structure with reduced porosity and thus reduced conductivity. Porosity in level ice has a different origin, mainly confined to vertical channels formed by percolating brine droplets. Level ice is thus vertical-to-horizontal anisotropic by a factor of ten, in favor of high vertical conductivity (Reid et al., 2006a).

An enhanced HEM ice-thickness retrieval method is needed to investigate the role of pressure ridges in the open sea and shallow coastal waters. Single-frequency systems are usually optimized to the frequency that is least sensitive to the ice conductivity (typically 4 kHz) and derives reliable ice thickness without multilayer inversion. The 3D forward modeling revealed in detail that the sounding depth of a 4 kHz signal is insufficient to resolve deep, highly porous ridge structures (Hendricks, 2009) and inversion studies showed that several appropriately distributed frequencies (e.g., 30 and 60 kHz as used by DFO) are needed to resolve ice conductivity (Pfaffling and Reid, 2009).

To further elucidate the frequency limitation, the commonly used HCP geometry is superior for layered structures, but has low sensitivity to lateral changes in geometry. Sea ice studies by Reid et al. (2003) or Liu and Becker (1990) compared HCP with coaxial or coplanar geometries and found better lateral resolution for horizontal-dipole systems due to the reduced footprints. The use of an additional, horizontal receiver component is expected to contribute significantly to the efficiency of using for 2D or 3D models in the data analysis. A combination of a vertical-transmitter dipole- and horizontal-receiver component will lead to comparable improvements as the actual footprint is determined by the interaction of induced and received field geometry (Reid and Vrbancich, 2004).

We used the 3D forward model to set a baseline for frequencies and sensitivities for the retrieval of true ridge thickness and porosity. The test scenario was accordingly given by a porous and grounded pressure ridge in water depth from 5 to 20 m and an HCP system at 12 m altitude. Grounded pressure ridges are typical features of land-fast sea ice in shallow coastal areas. These ridges govern the stability of the land-fast sea ice in the Arctic and Antarctic; however, they are of special interest in the Arctic, due to the socioeconomic use of this type of sea ice in the northern hemisphere. The conductivities were chosen to form a worst-case scenario with minimum conductivity contrast in the natural range between sea water, sea floor, and sea ice pressure ridge, respectively (sea water: 2.4 S/m, sea floor: 1 S/m, pressure ridge: 0.5 S/m). Note the relatively high ice conductivity (compared to 0.01 S/m for level ice) due to the increased ridge porosity. The geometry is based on a 2D cross section of a typical shape for a first-year Arctic pressure ridge (Timco and Burden, 1997) with a maximum thickness of 15 m (see Figure 1). At the surface, the ridge is 60 m wide and 7.5 m wide at the bottom. We found that at a frequency of 1 kHz, the EM response is sensitive to the lower part of the pressure ridge, whereas a lower frequency of 300 Hz is needed to resolve the depth of the water column below the ridge keel. Two higher frequencies (4 kHz, 10 kHz) were chosen for the model run to resolve the upper part of the ridge. In a second simulated overpass, we lowered the seafloor by 2 m, leaving the ridge structure unchanged. The grounding anomaly is defined as the difference between both simulations (Figure 2). We find that the sensor must have a sensitivity and accuracy below 10 ppm in amplitude and 0.5° in phase to resolve the grounding of ridges. The required sensitivity drops quickly in shallower cases (decreased pressure ridge thickness) or in cases where

the seafloor is more than 5 m below the keel of the pressure ridge, where the target is now defined only by the shape and porosity of the ridge.

## INSTRUMENTATION

To put MAiSIE in perspective, we briefly review the recent development of airborne EM systems dedicated for scientific sea-ice

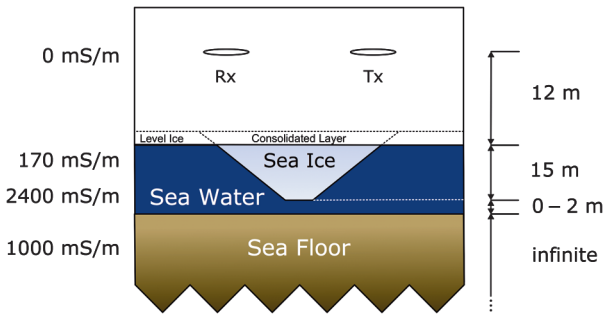


Figure 1. Cross section through 2D pressure ridge geometry used for the EM modeling study. The geometry of the ridge is typical of observed natural ridges (max width = 4 × thickness, min width = thickness/2). The HCP system height is a constant 12 m above the water table.

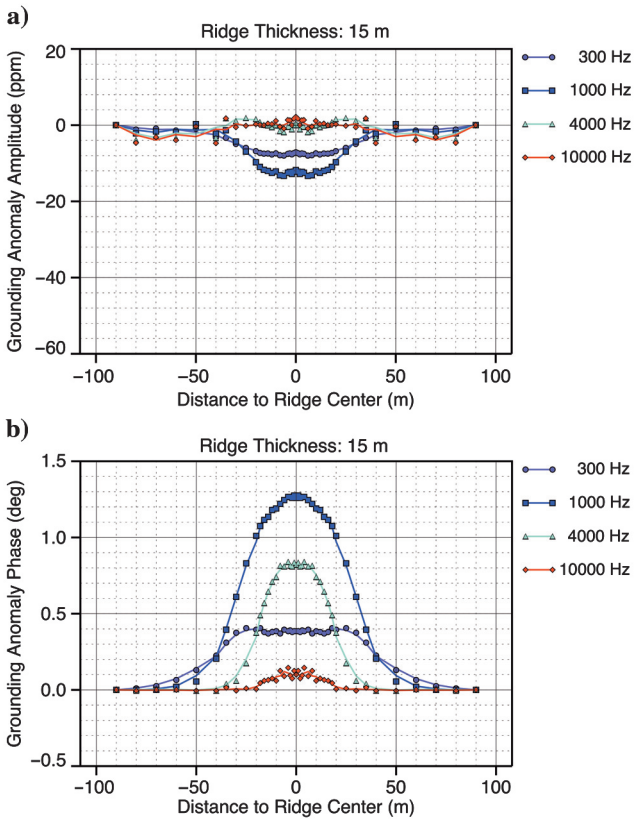


Figure 2. Ridge grounding anomaly (i.e., the difference in EM response for a grounded ridge compared to a floating ridge with 2 m water below the keel) for 15 m ridge thickness at signal frequencies 300 Hz to 10 kHz. The upper and lower panels show the normalized secondary field expressed as (a) amplitude and (b) phase component, respectively.

thickness mapping. Research institutes in Norway, China, and Canada have recently purchased systems equivalent to the small-scale bird developed by AWI (Pfaffling et al., 2004; Haas et al., 2006). AWI experimented with a fixed-wing adaptation with limited success (Rabenstein et al., 2011). The University of Alberta (Canada) is testing a dual-frequency (4 and 170 kHz) HEM system with integrated lidar scanner (C. Haas, personal communication, 2011). Key specifications of these sea-ice HEM systems are listed below:

1) Dimensions: Length 3.5 m, weight 100 kg
2) EM system: Single-frequency 4 kHz. Some systems use an additional frequency of 100–170 kHz. One coil set per frequency (transmitter loop at resonance frequency with capacitor bank), passive bucking, onboard calibration. Coil geometry horizontal coplanar: separation 2.0 m to 2.8 m
3) Auxiliary sensors integrated with EM: Laser altimeter, differential GPS, onboard data acquisition.
4) Operational details: Towing cable length 20–30 m, bird altitude 10–15 m above ice surface, speed 60–80 knots (approximately 30–40 m/s), system powered by the helicopter DC supply (28 V) and controlled by an operator using a laptop via WLAN.

To our knowledge, DFO still operates their proprietary helicopter sea-ice systems supporting ice charting and management in the Canadian Arctic. System development information after 1995 (Kovacs et al., 1995) is, however, limited to nonpeer-reviewed publications; e.g., Canadian contractor reports and conference proceedings. According to Peterson et al. (2003), the presently used 4.2 m long, towed-EM system (ice probe) operates at 30 and 90 kHz on one set of coils (an additional frequency of 150 kHz is not used due to noise and drift problems) in an HCP configuration combined with a laser altimeter and GPS-based orientation sensors. The system provides real-time ice-thickness data, as well as ice conductivity from postflight inversion. Test data including different ice types show good repeatability and agreement with borehole information (Peterson et al., 2003).

### MAiSIE System components

MAiSIE encompasses several features and components not possible with traditional simple state-of-practice systems, which we shall now describe in detail. As discussed in the "Sea-Ice Geophysics" section, introducing several frequencies and receiver components is expected to improve ice thickness estimates for 2D and 3D structures. We avoid erroneous ice-thickness results induced by attitude effects by virtue of a highly accurate INS and dual-antenna differential GPS solution. The multifrequency EM design and the broadband ferrite-core coil receivers enabled us to reduce the payload and allow additional sensors such as a cross-track lidar scanner and an infrared (IR) ice surface thermometer to be incorporated into the bird without exceeding its operational weight limit.

A detailed list of MAiSIE's system components is given below, and is shown schematically in Figure 3 (Dimensions and operational details are the same as those listed for traditional sea-ice HEM systems; 28 V DC power rating is 200 W).

1) EM system: Multifrequency system, freely programmable. One transmitter loop for all frequencies, current feedback transmitter amplifier, active digital bucking, onboard calibration. Coil

geometry: horizontal coplanar, fish tail, and whale tail (vertical dipole transmitter, three-axis receiver). Coil separation: 2.65 m.

2) Auxiliary sensors integrated with EM: Laser altimeter (Riegl LD 90), inertial navigation System (INS), combined with dual-antenna differential GPS (Novatel SPAN CPT and FlexPac-G2), lidar scanner (Riegl VQ580), IR ground surface thermometer (Heitronics KT19), onboard data acquisition (NI cRIO real-time controller and FPGA and single-board computer).

## EM concept

The EM system stands out with three main details: First, the transmitted signal is not limited to the L/C resonance frequency, as used traditionally, but rather follows a multifrequency concept, similar to Geophex's GEM-2A exploration system (Won et al., 2003) or the sea-ice systems tested by Kovacs and Holladay (1990) and operated in Canada (Peterson et al., 2003). Second, we apply a triplet of lightweight ferrite-core coils to acquire the secondary field in all directions $(x, y, z)$. The receivers were developed in cooperation with CNRS/Paris, based on a space-borne magnetometer developed by this research group (Coillot et al., 2010). Finally, we sample the transmitted EM field directly on the transmitter loop and use this signal to actively cancel (zeroing or bucking) the primary field by using a second set of windings integrated in the receiver coils, thereby actively bucking the primary field at the receiver location. This digital bucking is adjusted for every production flight during a bucking and calibration sequence at high altitude. Because we monitor the transmitted current directly on the $Tx$ loop, we can dynamically zero the primary field response and thus minimize drift due to $Tx$ instabilities. Rabenstein et al. (2011) discuss the advantages of dynamic bucking in greater detail.

We handle EM signal generation, acquisition, and processing with a real-time unit on an industrial FPGA-based reconfigurable input/output (RIO) system with digital and analog inputs and outputs (Figure 4). The analog input module used to sample the receiver voltages has 24-bit resolution, sampling at 25 kHz. The RIO composes the multifrequency EM signal by overlaying sine signals with the desired frequencies, which are in turn fed to the $Tx$ amplifier via a 16-bit analog output module. The same module provides the bucking turns in the receivers with the bucking signal, depending on the actual transmitter current. Real-time EM processing follows equation 1, providing calibrated and zeroed normalized secondary field $Z$ (following Ward and Hohmann, 1988)

$$Z = \frac{H_s}{H_p} = cal \times \frac{Rx - T \times Tx}{T \times Tx}, \tag{1}$$

with $H_p$ being the primary (field in a nonconductive full-space) and $H_s$ the secondary magnetic field strength (field above a conductive half-space arising from the eddy currents induced by the primary field). The sampled voltage on the receivers and transmitter current are expressed as $Rx$ and $Tx$, respectively. During high-altitude flights, the system's transfer function $T$ is determined as $H_s$ and is assumed to be negligible (i.e., zero) and thus $T = Rx/Tx$. Finally, the calibration factor cal is applied to account for all remaining uncertainties (inaccuracies in loop size and shape, dimensions, gain settings, etc.). The correct value for cal is established during calibration flights over deep water with known conductivity (Pfaffling and Reid, 2009). This fundamental system calibration is controlled during every flight by virtue of the onboard calibration coil, providing a known secondary field at the receivers. All variables leading to the normalized secondary field, equation 1, are complex numbers required separately for each active signal frequency and for each of the three receiver components.

## Data acquisition and user interface

The data acquisition (DAQ) architecture is split into a fully digital data-logging system handled by a single-board computer (SBC) and an RIO for EM-signal generation, acquisition, and processing (see section "EM concept"). These communicate via WLAN, ethernet,

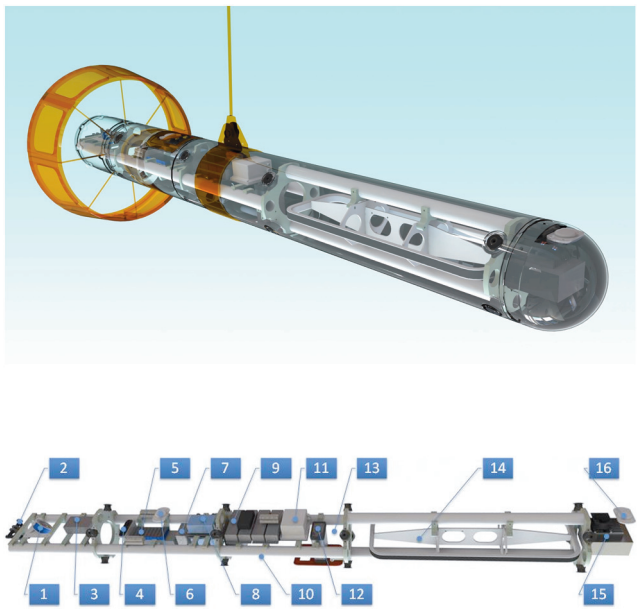


Figure 3. Design drawing showing main MAiSIE system components. From left to right and indicated in the legend; (1) calibration coil, (2) EM receiver coils, (3) $Rx$ amplifiers, (4) dual GPS receiver, (5) digital data acquisition and EM controller, (6 and 16) GPS antenna, (7) SBC, (8) AC/DC converters, (9) EM transmitter power supply, (10) space for laser scanner, (11) INS, (12) laser altimeter, (13) space for IR thermometer, (14) EM transmitter loop $30 \times 100$ cm, (15) EM transmitter amplifier. Total length of the fuselage is 3.5 m (11 ft), diameter 35 cm.

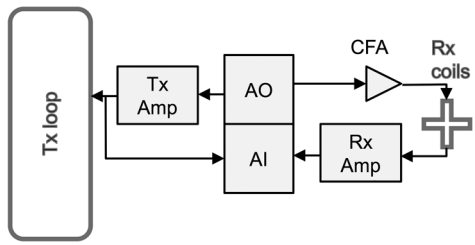


Figure 4. Schematics of major EM components. The EM waveform is fed from the 16-bit analog output (AO) to the transmitter amplifier ($Tx$ Amp) and through the transmitter loop ($Tx$ loop). The analogue input (AI) monitors the actual voltage and current in the $Tx$ loop to drive a closed feedback loop. Further, a current feedback amplifier (CFA) feeds the compensation signal from the AO into the $Rx$ coils triplet (active bucking). Finally, the compensated signal is amplified ($Rx$ ampere) and acquired by the 24 bit AI.

or optical fiber, with the operator computer running a graphical user interface (GUI) developed with LabVIEW. EM data is handled by the RIO in two ways: Raw 25 kHz streaming EM data is piped through to the SBC and logged there for postflight reanalysis, and 100 ms stacks are processed for each active signal frequency (complex division of receiver signals and transmitted current according to the real-time processing, equation 1), and provided as voltage amplitude and phase, as well as calibrated and zeroed/bucked in-phase and quadrature readings at 10 Hz. Beside logging the raw data series from the RIO, thermometer, altimeter, lidar scanner, INS, and dGPS, the SBC also carries out real-time processing tasks. To ensure efficient operation, we supply the operator's GUI with all crucial data to monitor during data acquisition. Real-time data from the various sensors are down-sampled to 10 Hz by the SBC and sent to the operator display. These real-time data include altitude, position and attitude, EM components $(x, y, z)$, EM transmitter current, and status messages to ensure that all components are operating as expected. The PPS signal (pulse per second) provided by the GPS is fed directly to the RIO, the SBC, and the lidar scanner to guarantee accurate timestamps throughout the system's individual sensors. Communication between the RIO, SBC, and scanner are ethernet based, and the other sensors are connected to the SBC via USB or RS232 (Figure 5).

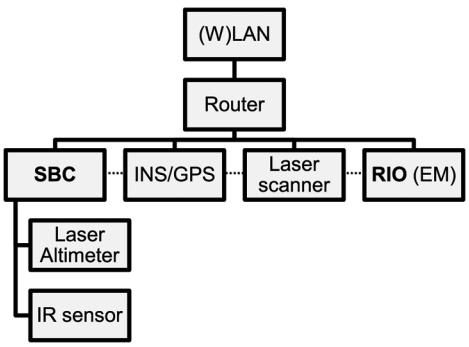


Figure 5. Data acquisition schematics. Black lines indicate data connection (Ethernet, RS232, or USB) between sensors and DAQ units (SBC and RIO). The stippled line indicates the direct PPS connection between GPS and laser scanner, SBC, and RIO for accurate time stamping. Streaming raw data from all five sensors is logged by the SBC and resampled to 10 Hz real-time data sent to the operator computer via WLAN.

Figure 6. Taking off for maiden flights in North Germany, towed by a twin-engine Bo 105.

## DATA QUALITY

The performance of the EM system was evaluated on 1 December 2011 during a test flight over the North Sea close to the German island of Helgoland (Figure 6). The scientific payload did not include a lidar scanner or IR thermometer, because the primary objective of the flight was the test of the EM subsystem. The test program consisted of periods at high altitude (>100 m) to monitor receiver and transmitter drift and two descents to operational altitude (10–15 m) with a multifrequency and a single-frequency EM configuration. The multifrequency configuration included four frequencies (0.5 kHz, 1.01 kHz, 4.1 kHz, and 7.95 kHz), whereas during the single-frequency mode only the 4.1 kHz was transmitted to test noise levels at the common frequency for 1D sea-ice thickness retrieval with a higher dipole moment.

The North Sea is an ideal test site due to the strong EM response of the ocean water, which has a higher salinity and temperature than surface waters of the Arctic Ocean. No in situ conductivity data was available during the test flight; therefore, we relied on previous measurements of ocean conductivity (4 S/m) at comparable surface water temperatures, given that salinity variations are typically small in the target area. The theoretical EM response of a half-space is always zero for the $y$-component (across-track) of the relative secondary field with a strictly vertical transmitter moment, due to the symmetry of the EM field. Therefore, significant roll angles of the bird up to 30° were induced by the helicopter pilot in parts of the profile to retrieve a measurable signal also on the receiver in $y$-direction.

Figure 7 shows an example of the recorded raw-EM signal at 4.1 kHz for all three receiver components. Displayed are the in-phase and quadrature components of the receiver signals in nanoTesla from a roughly eight-minute period. The EM response is evident in the sum of secondary and primary field $(H_s + H_p)$ and the residual primary field at the receivers $(H_p)$, or $Rx$ and $T * Tx$ used for real-time EM processing (equation 1). Further, the laser altitude and the INS pitch and roll angles show the steady flight segment (200–250 s) and the later induced roll movement (280–350 s). The response of the $x$- and $z$-components at lower altitudes and on the $y$-component at high roll angles is clearly visible. The noise levels of all three receiver components are comparable, while the induced signal is most pronounced on the $z$-component, as expected. Deviations from the primary signal at high altitude (0–100 s and 400 s — end) mark an additional secondary field, induced by closure of the onboard calibration loop.

We used low-pass filtering to reduce the initial noise levels of the raw signals. Then the transfer function $T$ (EM processing, equation 1) was calculated at altitudes higher than 60 m, where the secondary field from the ocean is negligible, by division of the recorded receiver $Rx$ and transmitter Tx voltages $(T = Rx/Tx)$. Periods where the calibration loop was closed were not included in the calculation of the transfer function. Results from the beginning and the end of the profile showed that the transfer function was not stable throughout the profile, most likely due to receiver drift. Tests showed that this drift was nonlinear, but could be sufficiently described by a second-order polynomial function. With the application of the transfer function in determining Z (equation 1) the signal is zeroed and corrected for sensor drift. To transform zeroed and drift corrected receiver reading to normalized secondary fields (ppm) a final calibration factor is needed (cal). For the $z$-component, the calibration factor can be calculated by comparing Z-values,

obtained by measured receivers and transmitter voltages and an arbitrary calibration (cal = 1), with the results from a 1D half-space model for a HCP configuration. As a 1D model, we used the code of Anderson (1979) with a half-space conductivity of 4 S/m and the altitudes measured by the single-beam laser altimeter. The calibration factor was subsequently calculated by division of the measured and modeled Z values (cal = Z modeled / Z measured). The attitude angles of the bird are not considered in this 1D forward model; therefore, data with roll angles >4° were excluded from the calculation of the calibration coefficient. The resulting Z in ppm for the $z$-component of 4.1 kHz frequency is shown with the 1D model result in Figure 8.

The data sets are generally in good agreement and do not reveal any visible sign of sensor drift (after correction with the second-order transfer function). The 1D model is visibly rougher at lower altitude, indicating that the sea surface was not an ideal 1D target. In fact, significant ocean swells with wave heights in the order of a few meters were observed by the operators in the helicopter. This effect might explain the spread of the measured signal around the modeled EM response, which can be seen on the right side of Figure 8.

Results from the other frequencies (not shown) show similar fundamental characteristics . Signal noise levels for single- and multifrequency tests are shown in Table 1. We note that the transmitted signal strength of each individual frequency depends on the weighting of its dipole moment in the EM configuration chosen by the operator. For example, the difference in signal strength of the 4.1 kHz frequency between the multifrequency and single-frequency mode is roughly a factor of three (Table 1). This difference should reduce the noise level by an equal factor. The noise level for all frequencies in both modes (multi- and single-frequency) is estimated as the standard deviation of Z at high altitude and in the absence of calibration pulses. In general, the noise levels in ppm of this initial test were higher than expected. The highest noise level is shown by the 0.5 kHz frequency (approx. 250 ppm), followed by the 1.01 kHz (approx. 120 ppm). The noise level of the higher frequencies are significantly smaller (around 20–40 ppm), but still quite high for the application to sea ice. The increase of the dipole moment of the 4.1 kHz frequency in the single-frequency mode did not result in lower noise levels, which indicates that this is not an effect of receiver sensitivity. Receiver sensitivity tests at CNRS also showed noise levels two to three orders of magnitude below the field levels. A visual inspection of the data at high altitude revealed that the noise is not a Gaussian-distributed high-frequency signal, but an oscillating perturbation most probably caused by unwanted interference with other frequency components. This effect is most prominent on the 1.01 kHz frequency, which shows a clear sinusoidal interference signal. Tests were made to ensure that all measured signals are properly zeroed and that the oscillating signal is not created by the initial low-pass filter. Without the filtering, the individual frequencies show doubled noise values. On the other hand, removal of the perturbating signal will reduce the noise level significantly to levels well within the design specifications below 10 ppm. Further, ground-based tests revealed that such harmonics are strongly dependent on the chosen signal frequency; e.g., 4 kHz is noisier than 4.1 kHz. Internal interference between the transmitter and bucking signals are a potential source for this coherent noise. Although we have successfully assessed the potential EM interference with the installed auxiliary sensors, the lidar scanner has not been tested to this date.

## DISCUSSION

We present a new realization of an airborne sea-ice thickness sensor with a capability for improved scientific payload and conduc-

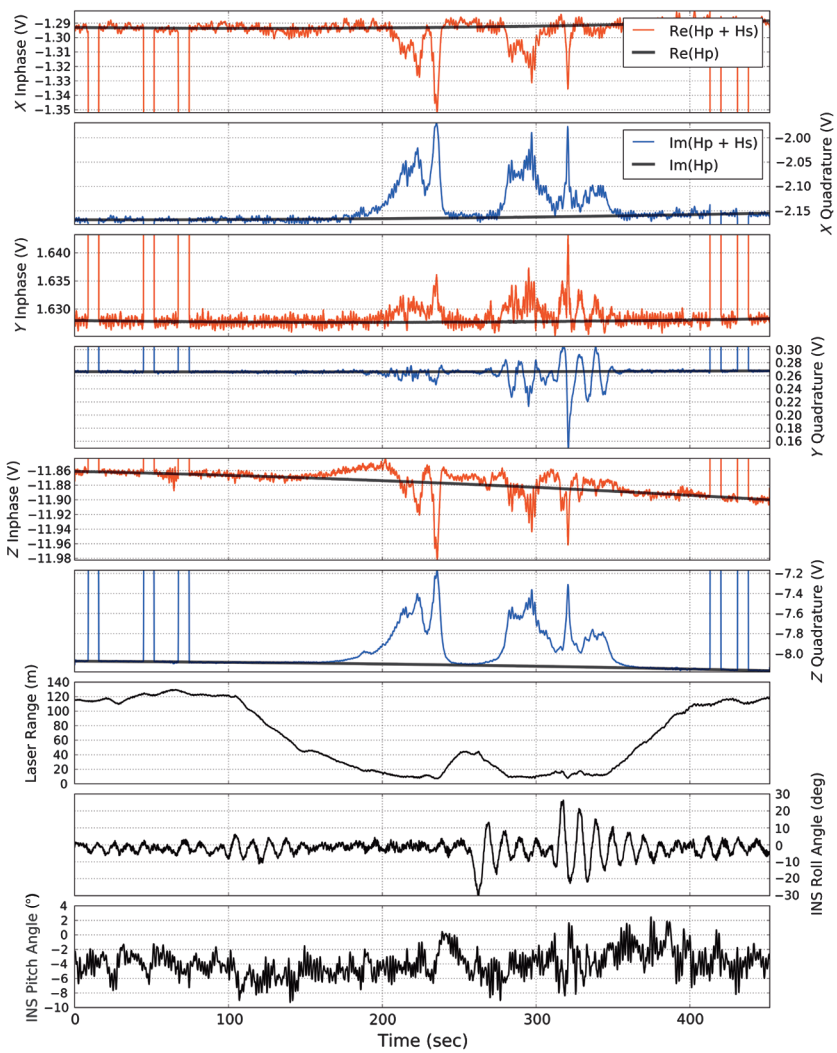


Figure 7. Example of raw data from all three receiver components $(x, y, z)$ of the inphase (red) and quadrature (blue) channels at 4.1 kHz in multifrequency mode (top six panels). The received voltages are provided as secondary and primary field (Hp + Hs) and the residual primary field (Hp) for about eight minutes. The lower three panels show the altitude measured by the single-beam laser altimeter and the roll and pitch angles sensed by the INS.

tivity soundings compared to existing instruments in the field of polar climate research. The stage of the project is now beyond the proof-of-concept, which has been reached with a test flight in December 2011. This test revealed the capabilities of a multifrequency and multicomponent EM configuration, but also showed room and need for further optimization. The most important step is the fine tuning (adjustment/shift) of the frequencies to minimize the effect of interference most likely caused by harmonics. The acceptable noise level is determined by the desired ice-thickness accuracy and precision as well as system sensitivity. At 15 m altitude, 10 ppm noise leads to approximately 10 cm thickness precision; at 13 m altitude, 20 ppm noise can be tolerated, resulting in 10 cm ice-thickness precision (Pfaffling et al., 2007). MAiSIE has thus delivered sufficient data quality for sea-ice thickness retrieval. The desired 10 ppm noise level for pressure ridge grounding (see section "3D EM modeling") has not been met yet, however. Sensor drift seems to be under control during data acquisition; however, the system has not yet been operated in environmental conditions of Arctic spring with air temperatures well below –20°C. Therefore, sensor-drift correction techniques by means of temperature recording of EM components or the use of weak unbucked signals, which mainly contain the primary field, have to be developed to control nonlinear drift. Temperature sensors are distributed on key sensors in the bird to be ready for this development. The next step to improved sea-ice thickness retrievals is the development of an adapted inversion algorithm which uses the full capacity of the multicomponent receiver.

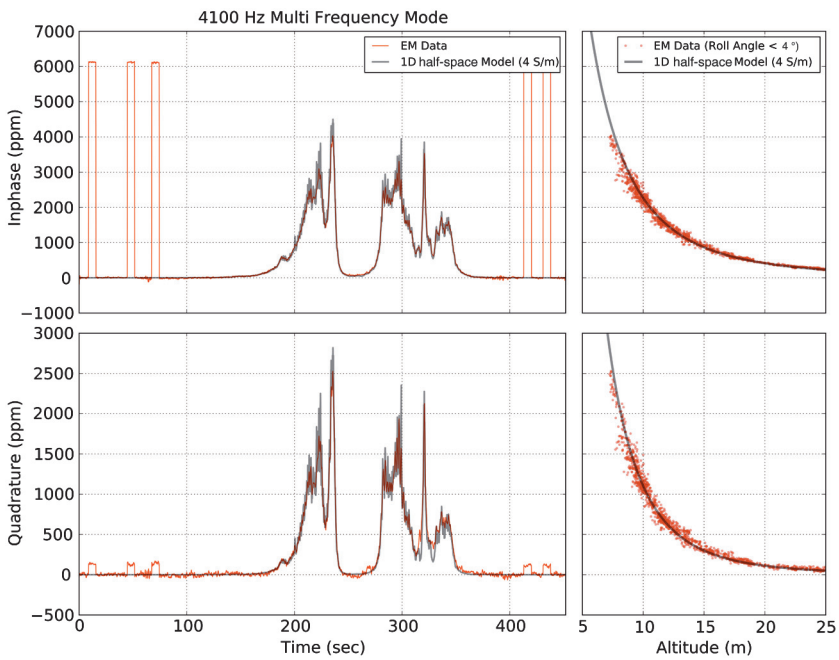


Figure 8. Calibrated and modeled EM response over water ($z$-component only) given by in-phase (red) and quadrature (blue) channels at 4.1 kHz in multifrequency mode. The panels on the left side show the comparison of measured and modeled data along the profile; on the right side, the comparison is given as a function of instrument height above the water.

Climate research not only needs improved data sets, but primarily consistent long-term records of climate variables with associated uncertainties. The MAiSIE system represents one step in this direction, because it gives the prospect of improved but also coincident traditional 1D sea-ice thickness retrieval. We plan to assess these uncertainties over different types of sea ice, which consequently can be translated into uncertainties relating to all existing airborne EM ice thickness data. Here, the three receiver components are of central importance even without a 2D or 2.5D inversion, because the distribution of full-component secondary field gives information over the dimensionality of the sea-ice medium and the validity and associated error of the 1D assumption. Ultimately, only full 3D and/or 2D inversion will provide the added value from the multicomponent data. Because sea ice features distinct boundaries, a geometry based inversion will likely provide best results over traditional smooth inversion with respect to pressure ridge thickness.

We expect the first operational use of MAiSIE in the Arctic in spring 2012. Several field campaigns have to follow; however, the initial test data presented here offer the promise that our goals of improved airborne sea-ice thickness retrieval can be achieved with the existing prototype instrument.

**Table 1. Signal noise levels (given by the standard deviation at high altitude) for all frequencies in both instrument modes (multi- and single-frequency) for the in-phase and quadrature components of the relative secondary field Z in ppm. Desirable for sea ice applications are noise levels below 10 ppm in the frequency range of 1 to 8 kHz, leading to 10 cm thickness precision at 15 m flight height.**

| Frequency (Hz) | Transmitter moment (NIA) | Noise in-phase (ppm) | Noise quadrature (ppm) |
|---|---|---|---|
| | *Multifrequency mode* | | |
| 500 | 12.6 | 240 | 257 |
| 1010 | 12.6 | 114 | 124 |
| 4100 | 25.2 | 20 | 18 |
| 7950 | 6.3 | 33 | 49 |
| | *Single-frequency mode* | | |
| 4100 | 63 | 21 | 16 |

## CONCLUSION

We have shown that it is possible to increase the number of sensors on a relatively small airborne instrument by a fundamental redesign of the EM concept. Using a single transmitter loop for all frequencies, omitting a passive bucking coil, and using a small and light ferrite-core magnetometer triplet as receivers, we significantly reduced the weight of the EM subsystem. Sea-ice mapping is a particular objective that motivates such a development to map various parameters from one platform. Acquisition of transmitter current and receiver voltages allows real time active bucking by virtue

of a system transfer function. A consequent time-variant adaptation of the transfer function during postprocessing leads to drift-corrected EM data.

We illustrate the development phase of a new generation of AEM systems for accurately measuring sea-ice thickness, including the thickness of pressure ridges using 2D/3D EM interpretation software. This represents the first step to enable this climate-critical parameter to be accurately mapped. Test flights have delivered satisfactory data for a proof-of-concept, yet full-scale operational testing is pending until April 2012. Initial test flight noise levels are not fully satisfactory, and further work is needed to reduce potential internal interferences leading to decreased data quality.

Subsets of the components implemented in MAiSIE have been used before in commercial exploration systems and sea-ice mapping systems; however, no system has yet combined all components in one bird. Findings gained from our presented research could also improve operational exploration systems. Most significantly, the lightweight, multicomponent EM receiver concept offers new opportunities for EM induction systems.

MAiSIE has the potential to become a landmark in polar research, and to provide the basis for a new generation of systems. The accuracy of final data deliverables from MAiSIE will hopefully improve significantly over equivalent deliverables obtained from traditional sea-ice EM sensors.

## REFERENCES


ACIA, 2004, Impacts of a warming arctic: Arctic climate impact assessment: Cambridge University Press, ISBN: 0521617782.

Anderson, W., 1979, Numerical integration of related Hankel transforms of order 0 and 1 by adaptive digital filtering: Geophysics, **44**, 1287–1305, doi: 10.1190/1.1441007.

Beamish, D., 2003, Airborne EM footprints: Geophysical Prospecting, **51**, 49–60, doi: 10.1046/j.1365-2478.2003.00353.x.

Coillot, C., J. Moutoussamy, R. Lebourgeois, S. Ruocco, and G. Chanteur, 2010, Principle and performance of a dual-band search coil magnetometer: A new instrument to investigate fluctuating magnetic fields in space: IEEE Sensors Journal, **10**, 255–260, doi: 10.1109/JSEN.2009.2030977.

Davis, A. C., J. Macnae, and T. Robb, 2006, Pendulum motion in airborne HEM systems: Exploration Geophysics, **37**, 355–362, doi: 10.1071/EG06355.

Fitterman, D. V., and C. Yin, 2004, Effect of bird maneuver on frequency-domain helicopter EM response: Geophysics, **69**, 1203–1215, doi: 10.1190/1.1801937.

Haas, C., S. Goebell, S. Hendricks, T. Martin, A. Pfaffling, and C. von Saldern, 2006, Airborne electromagnetic measurements of sea-ice thickness: Methods and applications: in P. Wadhams, and G. Amanatidis, eds., European commission, Arctic sea-ice thickness: Past, present & future, Brussels, Climate change and natural hazards series.

Hendricks, S., 2009, Validation of altimetric sea-ice thickness measurements with a helicopter based electromagnetic induction method: Ph.D. thesis, (in German), University of Bremen.

Holladay, J. S., and S. K. Prinsenberg, 1997, Bird orientation effects in quantitative airborne electromagnetic interpretation of pack ice thickness sounding: Oceans '97, Marine Technology Society Institute of Electrical and Electronic Engineers conference proceedings, **2**, 1114–1116.

Holladay, J. S., J. R. Rossiter, and A. Kovacs, 1990, Airborne measurements of sea-ice thickness using electromagnetic induction sounding: 9th Conference of Offshore Mechanics and Arctic Engineering, conference proceedings, 309–315.

Kovacs, A., and J. S. Holladay, 1990, Sea-ice thickness measurement using a small airborne electromagnetic sounding system: Geophysics, **55**, 1327–1337, doi: 10.1190/1.1442780.

Kovacs, A., S. Holladay, and C. J. Bergeron Jr., 1995, The footprint/altitude ratio for helicopter electromagnetic sounding of sea-ice thickness: Comparison of theoretical and field estimates: Geophysics, **60**, 374–380, doi: 10.1190/1.1443773.

Kovacs, A., and R. M. Morey, 1991, Sounding sea-ice thickness using a portable electromagnetic induction instrument: Geophysics, **56**, 1992–1998, doi: 10.1190/1.1443011.

Kovacs, A., N. C. Valleau, and J. S. Holladay, 1987, Airborne electromagnetic sounding of sea-ice thickness and subice bathymetry: Cold Regions Science and Technology, **14**, 289–311, doi: 10.1016/0165-232X(87)90021-8.

Kwok, R., and G. F. Cunningham, 2008, ICESat over arctic sea-ice: Estimation of snow depth and ice thickness: Journal of Geophysical Research, **113**, C08010, doi: 10.1029/2008JC004753.

Lindsay, R., 2010, New unified sea-ice thickness climate data record: EOS, **91**, 405–406.

Liu, G., and A. Becker, 1990, Two-dimensional mapping of sea ice keels with airborne electromagnetics: Geophysics, **55**, 239–248, doi: 10.1190/1.1442832.

Liu, G., A. Kovacs, and A. Becker, 1991, Inversion of airborne electromagnetic survey data for sea-ice keel shape: Geophysics, **56**, 1986–1991, doi: 10.1190/1.1443010.

Multala, J., H. Hautaniemi, M. Oksama, M. Lepparanta, J. Haapala, A. Herlevi, K. Riska, and M. Lensu, 1996, An airborne system on a fixed-wing aircraft for sea-ice thickness mapping: Cold Regions Science and Technology, **24**, 355–373, doi: 10.1016/S0165-232X(96)00006-7.

Peterson, I. K., S. J. Prinsenberg, and J. S. Holladay, 2003, Sea-ice thickness measurement: Recent experiments using helicopter-borne EM-induction sensors: Research Signpost India, Recent Research Developments in Geophysics, **5**, 1–20.

Pfaffling, A., C. Haas, and J. E. Reid, 2004, Empirical processing of HEM data for sea-ice thickness mapping: 10th EEGS, Expanded Abstracts, A037.

Pfaffling, A., C. Haas, and J. E. Reid, 2007, A direct helicopter EM sea-ice thickness inversion, assessed with synthetic and field data: Geophysics, **72**, no. 4, F127–F137, doi: 10.1190/1.2732551.

Pfaffling, A., and J. E. Reid, 2009, Sea ice as an evaluation target for HEM modeling and inversion: Journal of Applied Geophysics, **67**, 242–249, doi: 10.1016/j.jappgeo.2008.05.010, doi: 10.1016/j.jappgeo.2008.05.010.

Prinsenberg, S. J., J. S. Holladay, and J. Lee, 2002, Measuring ice thickness with EISFlow™, a fixed-mounted helicopter electromagnetic-laser system: 12th International Offshore and Polar Engineering Conference, Conference Proceedings, **1**, 737–740.

Rabenstein, L., S. Hendricks, J. Lobach, and C. Haas, 2011, Noise characteristics of an electromagnetic sea-ice thickness sounder on a fixed wing aircraft: Journal of Applied Geophysics, **75**, (1), 87–98, doi: 10.1016/j.jappgeo.2011.06.006.

Reid, J. E., A. Pfaffling, and J. Vrbancich, 2006b, Airborne electromagnetic footrpints in 1D earths: Geophysics, **71**, no. 2, G63–G72, doi: 10.1190/1.2187756.

Reid, J. E., A. Pfaffling, A. P. Worby, and J. R. Bishop, 2006a, In situ measurements of the direct-current conductivity of Antarctic sea ice: Implications for airborne electromagnetic sounding of sea-ice thickness: Annals of Glaciology, **44**, 217–223, doi: 10.3189/172756406781811772.

Reid, J. E., and J. Vrbancich, 2004, A comparison of the inductive-limit footprints of airborne electromagnetic configurations: Geophysics, **69**, 1229–1239, doi: 10.1190/1.1801939.

Reid, J. E., J. Vrbancich, and A. P. Worby, 2003, A comparison of shipborne and airborne electromagnetic methods for Antarctic sea-ice thickness measurements: Exploration Geophysics, **34**, 46–50.

Singarayer, J. S., J. L. Bamber, and P. J. Valdes, 2006, Twenty-first-century climate impacts from a declining Arctic sea ice cover: Journal of Climate, **19**, (7), 1109–1125, doi: 10.1175/JCLI3649.1.

Sinha, A. K., 1976, A field study for sea-ice thickness determination by electromagnetic means: Geological Survey of Canada, Paper 76 (1C), 225–228.

Timco, G., and R. Burden, 1997, An analysis of the shapes of sea ice ridges: Cold Regions Science and Technology, **25**, 65–77, doi: 10.1016/S0165-232X(96)00017-1.

Ward, S. H., and G. W. Hohmann, 1988, Electromagnetic theory for geophysical applications, *in* M. N. Nabighian, eds., Electromagnetic methods in applied geophysics, vol. 1, theory: SEG, 131–311.

Wingham, D., C. Francis, S. Baker, C. Bouzinac, D. Brockley, R. Cullen, P. Chateau-Thierry, S. Laxon, U. Mallow, C. Mavrocordatos, L. Phalippou, G. Ratier, L. Rey, F. Rostan, P. Viau, and D. Wallis, 2006, CryoSat: A mission to determine the fluctuations in earths's land and marine ice fields: Advances in Space Research, **37**, 841–871, doi: 10.1016/j.asr.2005.07.027.

Won, I. J., A. Oren, and F. Funak, 2003, GEM-2A: A programmable broadband helicopter-towed electromagnetic sensor: Geophysics, **68**, 1888–1895, doi: 10.1190/1.1635041.